Journal of Materials Chemistry A

Catalyzing Zinc-ion Intercalation in Hydrated Vanadates for Aqueous Zinc-ion Batteries

Journal:	*Journal of Materials Chemistry A*
Manuscript ID	TA-ART-02-2020-001468.R1
Article Type:	Paper
Date Submitted by the Author:	17-Mar-2020
Complete List of Authors:	Liu, Chaofeng; University of Washington, Materials Science and Engineering Tian, Meng; University of Washington Wang, Ming-Shan; University of Washington Zheng, Jiqi; University of Washington Wang, Shuhua; Shandong University Yan, Mengyu; University of Washington, Materials Science and Engineering Department Wang, Zhaojie; University of Washington Yin, Zhengmao; Qingdao University of Science and Technology Yang, Jihui; University of Washington, Materials Science and Engineering Cao, Guozhong; University of Washington, Materials Science and Engineering

Catalyzing Zinc-ion Intercalation in Hydrated Vanadates for Aqueous Zinc-ion Batteries

Chaofeng Liu,[a] Meng Tian,[a] Mingshan Wang,[a] Jiqi Zheng,[a] Shuhua Wang,[b] Mengyu Yan,[a] Zhaojie Wang,[a] Zhengmao Yin,[c] Jihui Yang, [a*] Guozhong Cao [a*]

[a] Department of Materials Science and Engineering, University of Washington, Seattle, WA, USA, 98195

[b] Institute of Crystal Materials, Shandong University, Jinan, China, 250100

[c] College of Materials Science and Engineering, Qingdao University of Science and Technology, Qingdao, China, 266042

Corresponding authors: J. Yang (jihuiy@uw.edu) and G.Z. Cao (gzcao@uw.edu)

Abstract

Hydrated vanadium pentoxide (VOH) can deliver a gravimetric capacity as high as 400 mAh/g owing to the variable valence states of V cation from 5+ to 3+ in an aqueous zinc ion battery. Incorporation of divalent transition metal cations has demonstrated to overcome the structural instability, sluggish kinetics, fast capacity degradation, and serious polarization. The current study reveals that the catalytic effects of transition metal cations are likely the key for the significantly improved electrochemical properties and battery performance because the higher covalent character of 55% in Cu-O bond in comparison with 32% of Mg-O bond in the respective

samples. Cu (II) pre-inserted VOH (CuVOH) possesses much enhanced intercalation storage capacity, increased discharge voltage, great transport properties, and reduced polarization, while both VOH and Mg (II) pre-inserted VOH (MgVOH) demonstrate similar electrochemical properties and performance, indicating that the incorporation of Mg cations has little or no impacts. For example, CuVOH has a redox voltage gap of 0.02 V, much smaller than 0.25 V of VOH and 0.27 V of MgVOH. CuVOH shows an enhanced exchange current density of 0.23 A/g, compared to 0.20 A/g of VOH and 0.19 A/g of MgVOH. CuVOH delivers a zinc ion storage capacity of 379 mAh/g, higher than 349 mAh/g of MgVOH and 337 mAh/g of VOH at 0.5 A/g. CuVOH performs an energy efficiency of 72%, superior to 53% of VOH and 55% of MgVOH. All the results suggest that pre-inserted Cu (II) cations played a critical role in catalyzing the zinc ion intercalation reaction while Mg (II) cations did not exert detectable catalytic effect.

Keywords: hydrated vanadates, transition metal cations, catalytic effect, Zinc ion batteries, exchange current density

Introduction

Further development of efficient energy conversion technologies to harvest renewable energy from sunlight, biomass, wind and tide energy has attracted more attention because of the increasing energy demand and environmental concerns with the population explosion and the surging industrial development in modern society.[1-3] Energy storage system (EES) is one of the

important enablers. Rechargeable batteries and supercapacitors are the two main categories in EES, the former stores electricity as chemical energy through a redox reaction in their electrode materials and the later utilizes the fast physical adsorption of ions on the surface of the electrode materials.[4-6] The differences in charge storage mechanism endow batteries with high energy densities and supercapacitors with high power densities.[4, 7, 8] For example, the mature Li-ion batteries promote the popularity of smart electronics and electric vehicles in modern society owing to their energy densities exceeding 250 Wh/kg, even though the challenges on interface issues and safety as well as reliability still remain.[9, 10] Aqueous zinc ion batteries (ZIBs) become a viable member of EES because the nonflammable electrolytes ensure their operating safety, the redox reaction provides moderate energy density, and feasible de-solvation and rapid diffusion of zinc ions in the active materials guarantee their high power densities.[11-14] Comparing with the nonaqueous Li- or Na-ion batteries, ZIBs are safer and more cost effective. To improve the competitiveness of ZIBs on energy density, searching for cathode materials with high discharge voltage and large storage capacity becomes one of the important priorities. Currently, the most commonly investigated cathode materials for ZIBs include manganese oxides,[15-24] vanadium oxides,[25-34] Prussian blue and its analogies,[35-38] transition metal sulfides[39-41] and organic compounds.[42] In manganese dioxides, an essential member of the Mn-based cathodes, the stacking of [MnO_6] polyhedra bestows different chemical activity and ion diffusion channels[43, 44]. The partially irreversible phase transition and dissolution of Mn^{3+} cause a rapid capacity degradation,[45, 46] though they display a relatively high working voltage around 1.3 V.[15] Prussian blue and its analogies have an open framework beneficial to fast ion diffusion but the less variable chemical state of the redox ions limits their specific capacity to < 100 mAh/g.[36] The weak Van de

Waals interactions between the layers of metallic sulfides facilitate zinc ion diffusion, but the serious voltage polarization in the charging/discharging processes leads to a lower battery energy efficiency that limits their practicability.[39, 41] Organic compound calix[4]quinone (C4Q) as a promising cathode candidate displays a safe and flat working voltage of 1 V, and low polarization of 70 mV; however, the dissolution of discharge products remains a challenge.[42] Vanadium oxides and their hydrates attract more attention owing to their high specific capacity up to 400 mAh/g, high power density enabled by a fast ion diffusion in the crystalline lattice, and low cost due to the abundance of vanadium in the Earth's crust.[26, 29, 30, 33, 47-50] Layered V_2O_5 chunks exfoliate to thin layers which increase the active sites and present an increased specific capacity in the cycling process[26] and the structural water in graphene/V_2O_5 composite shields the electrostatic interactions between cations and accelerates zinc ion transport, leading to an impressive power density in a battery.[29, 51] Alkali(ne) preinserted hydrated vanadium pentoxide effectively expands the lattice spacing to provide a highway for ion diffusion in the electrochemical processes.[31, 47, 52] These approaches overcome either the structural instability or sluggish kinetics, but seldom triumph over both challenges together. Transition metal (TM) compounds are used as catalysts for oxygen and hydrogen generation owing to the electrons in their 3*d* orbitals[53] and the electrochemical catalytic effect is widely introduced into Li-S batteries to restrain the dissolution of polysulfides.[54, 55] However, the impacts of transition metal cations on hydrated vanadium pentoxides are not clear, especially their stabilizing and catalytic effects on Zn-ion storage reactions.

Our earlier work has demonstrated Mn (II) cations as structural pillars expand the lattice spacing of VOH to accelerate ion diffusion and stabilize the crystal structure, promoting energy efficiency with an increase of 70% and the capacity retention around 92% at 4 A/g over 2,000 cycles.[56] This study compares Cu (II) pre-inserted hydrated vanadium pentoxides (CuVOH) with pure VOH and Mg (II) pre-inserted VOH (MgVOH), and reveals that chemically pre-inserted Cu (II) cations catalyzes the redox reaction and improves the reactive kinetics with much less polarization, resulting in much improved battery performance including increased energy and power densities, better cycling stability and higher energy conversion efficiency.

Experimental

All chemicals were used as received without purification. 2 mmol of V_2O_5 (Sigma-Aldrich) was dissolved into 50 mL of DI H_2O with 2 mL of H_2O_2 (30%, Fisher chemical), and 1 mmol of $CuSO_4 \cdot 5H_2O$ (Fisher scientific) was dissolved separately into 30 mL of DI water. Two solutions were admixed and transferred to a 100 mL Teflon lined stainless steel autoclave and heated to and held at 120 °C for 6 h. Brick red precipitates were collected by centrifugation and washed by water and ethanol for three times. The collected precipitates were dried at 70 °C overnight in an electric oven and turned greenish. The resulting product (CuVOH) was further dried at 120 °C in a vacuum oven. VOH was synthesized with the same procedure and processing conditions without the Cu (II) source, 80 mL of DI water was used in order to attain the same internal reactive pressure in the Teflon bottle. For Mg (II) stabilized VOH, its sulfate salts were used to synthesize the desired samples and the processes were identical to that of the CuVOH synthesis.

Phase identification was carried out by a Bruker X-ray diffractometer (D8 Discover with IμS 2-D detection system) with an accelerating voltage of 50 kV and a working current of 1000 μA. A Renishaw InVia Raman Microscope equipped with the Leica DMIRBE inverted optical microscope was used to obtain the chemical bond information by one of the laser excitation sources at 514 nm. A thermogravimetric analysis/differential scanning calorimeter (TGA/DSC 3+ STAR^e System, Mettler Toledo) was adopted to analyze the water content of the samples within 30-700 ˚C in a flowing nitrogen gas (50 sccm). The microstructures of samples were observed by a scanning electron microscope (SEM, FEI Sirion) at a working voltage of 5 kV and a scanning transmission electron microscope (S/TEM, Tecnai G2 F20) with an accelerating voltage of 200 kV. Inductively Coupled Plasma (ICP, PerkinElmer, Optima2000DV) was used to confirm the content of metal elements in the samples. The surface chemical states of samples were determined using a Kratos Axis Ultra DLD X-ray Photoelectron Spectroscopy system (XPS) with an AlKα radiation source that was operated at 10 mA and 15 kV, and with a charge neutralizer. The angle between the specimen normal and the spectrometer was 0˚. The chemical surroundings and states in bulk samples were detected by X-ray absorption near edge structure (XANES) by means of an improved laboratory-based instrumentation. The powder samples were admixed with boron nitride (BN) binder and tableted before conducting transmission-mode measurements. Commercial VO_2 and V_2O_5 purchased from Alfa Aesar were confirmed by XRD and used as reference standards.

For the electrode preparation, the active material was mixed with conductive carbon and polyvinylidene fluoride (PVDF) binder in a weight ratio of 7:2:1 in N-Methyl-2-Pyrrolidone (NMP) solvent to obtain a slurry that was pasted on a current collector - titanium foil. The prepared electrodes were dried in a vacuum oven at 120 °C overnight. The mass loading of active materials is 3 - 4 mg/cm^2. Zn metal was used as the anode and 80 μL of 3 M zinc trifluoromethanesulfonate (98%, $Zn(CF_3SO_3)_2$) aqueous solution was injected into the batteries as the electrolyte. A glass fiber filter (Whatman, Grade GF/A) was used as the separator. The redox characteristics of cathodes were tested by cyclic voltammogram (CV) on a Solartron electrochemical station (SI 1287) equipped with an electrochemical impedance spectroscopy system (EIS, SI 1260). The Galvanostatic charge and discharge tests were conducted using a Neware tester (CT-4008). Galvanostatic intermittent titration technique (GITT) was applied to analyze the reaction resistance in the electrochemical process and the tests was performed at a current density of 50 mA/g with a charging and discharging time and interval of 10 min for each step.

Results and discussion

Figure 1a shows and compares X-ray Diffraction (XRD) patterns of CuVOH, MgVOH and VOH. For VOH, it can be well indexed to $V_2O_5{\cdot}1.6H_2O$ (PDF 40-1296) and the (001) peak at 7.4° corresponds to an interplanar spacing of 11.9 Å, as reported in literature.[57] CuVOH and MgVOH have similar XRD patterns, matching two structures reported.[58-60] One is $M_xV_2O_5A_y{\cdot}nH_2O$, in which M (cations), A (anions) and water reside in stacked vanadium-oxide double layers.[58] The other is $M_xV_2O_{5+y}{\cdot}nH_2O$ that also has a layered structure and M cations are believed to replace the

protons in the original structure of the layered hydrated vanadic acids by an electrodeposition process with some peaks indexed in the literatures.[59, 60] The (001) peaks of CuVOH and MgVOH at 7.9 and 6.7° indicate an interplanar spacing of 11.2 and 13.2 Å, respectively. Cu (II) has an ionic radius of 87 pm, very close to 86 pm of Mg (II), thus the radii of cations are unlikely the determining factor for the change of the interplanar spacing. The electronegativities of Cu and Mg are 1.90 and 1.31 Pauling scale, respectively, therefore we speculate different interactions between the cation and VOH induce the varied compactness along the *c*-direction. Although it is believed that the lattice spacing will be expanded when cations are introduced, as reported on alkali(ne) preinserted VOH,[31, 47] the formation of chemical bonds may have varied impacts on the interplanar spacing. Raman spectra in Figure 1b exhibit similar characteristic peaks among all samples. The peaks around 159 cm^{-1} originate from the bending vibration of the -V-O-V-O- chains along the *a*-directional and cause a compressive deformation in the planes.[61] Terminal O and center V form a V=O double bond and its bending vibration is reflected by the peak at 264 cm^{-1}.[62] The vibrational motion of lattice water appears at 352 cm^{-1}. A stretching signal at 512 cm^{-1} comes from a V-O bond in which the O is triply coordinated by V cations and connects three VO_5 pyramids in the lattice.[62, 63] Another V-O bond built by a bridging O with two V cations from apical-sharing VO_5 pyramids is manifested by a stretching vibration at 706 cm^{-1} and the disorder of this V-O bonds in the lattice can be detected by the stretching vibration at 674 cm^{-1}.[62, 64] The peak at 891 cm^{-1} is attributed to the stretching of V-OH_2, and an upshift in CuVOH means the rotational freedom of water is limited, which might be caused by a strong Cu-O bond consistent with the narrow-spaced (001) planes verified by XRD in Figure 1a. The green rectangles in the CuVOH spectrum were enlarged and simulated by Lorentz functions. The bending mode of Cu-

O bonds is observed at 646 and 326 cm^{-1}, suggesting the introduced Cu (II) connects to the VO_5 pyramids through a chemical bond[65-67] rather than the weak hydrogen bonds between water and VO_5 pyramids.[68] The overlap between Cu-O and V_2-O suggest the interaction between Cu (II) and the bridging oxygen in [VO_5] polyhedral, and that the Cu (II) also interacts with water as shown at 326 cm^{-1} in the Raman spectra. It can be speculated that Cu (II) resides in the polyhedra built by the bridging oxygen and water as shown in Figure 1c. The electrostatic forces among cations including V^{5+}, V^{4+} and Cu (II) might result in alternative occupations as marked by the solid blue spheres or the dashed blue circles. The overlapping signals of bending vibration of Mg-O at 855 cm^{-1} [69] with the signal of V-OH_2 at 891 cm^{-1} result in a broad peak in MgVOH, suggesting the chemical bonds also forms among Mg (II), water and apical oxygen in the [VO_5] polyhedra. The similarities in Raman spectra and the differences in XRD patterns suggest CuVOH and MgVOH are likely to have a similar crystal structure as VOH and the introduced divalent cations in the interplane form chemical bonds because the pre-insertion of cations seldom cause a noticeable difference in the XRD patterns, such as the case for Li^+ [31]and Mg^{2+} [47] pre-insertion. Inductively coupled plasma (ICP) measurements confirm the atomic ratios of Cu: V and Mg: V are 0.091:1 and 0.080:1, respectively, suggesting the chemical formula of both samples can be written as $Cu_{0.15}V_2O_{5+\delta}\cdot nH_2O$ and $Mg_{0.14}V_2O_{5+\delta}\cdot nH_2O$, respectively. The concentration of Cu(II) cation the resulting samples would not be adjusted, though the molar ratio of $CuSO_4$ and V_2O_5 was varied from 1:20 to 1:2. Increasing the concentration of Cu (II) could increase the product yield but not influence its phase (Figure S1).

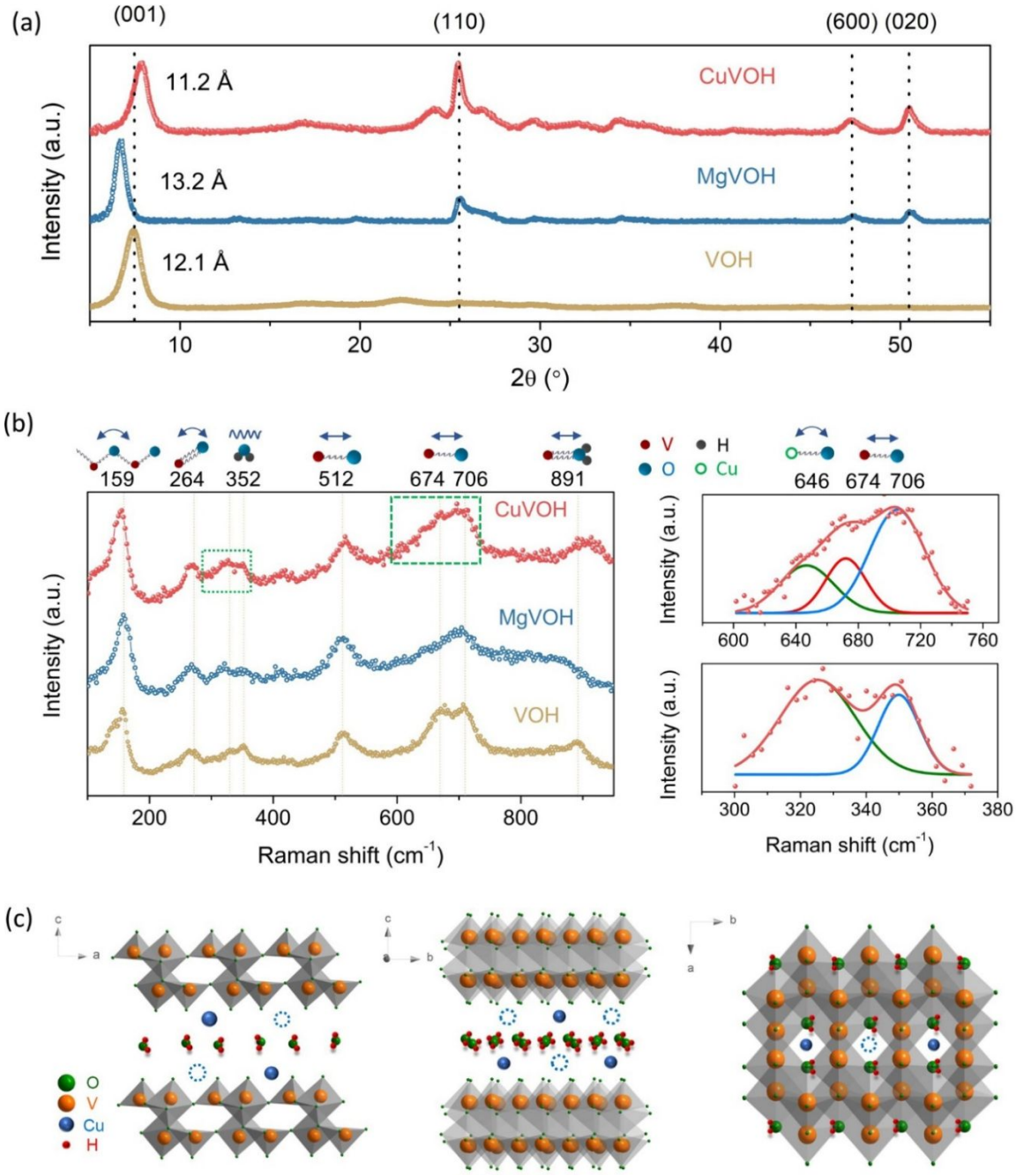

Figure 1. (a) XRD patterns of three samples with the (001) peak around 7.4°. VOH samples with chemically inserted divalent cations present similar XRD patterns though a few minor additional peaks appear in comparison with VOH. (b) Raman spectra of the samples with some peak shifts. The signals from Cu-O bond stretch and vibration suggest Cu (II) is connected and incorporated to the lattice. (c) Schematic of the possible Cu (II) occupation sites in the framework of VOH based on the analysis of the interactions among V, Cu, and O. The probable position for Cu (II) is in the polyhedra built with the bridging O from [VO_5] and water.

Table 1. Physical parameters of stabilized VOH

Sample ID	MgVOH	CuVOH
Interplanar spacing of (001) (Å)	13.2	11.2
Ionic radius of the divalent cation (pm)	86 (Mg)	87 (Cu)
Electronegativity of element (Pauling scale)	1.31 (Mg)	1.90 (Cu)
The amount of V^{4+} (%)	16.5	17.9

Figure S2 displays the scanning electron microscopy (SEM) images, showing all samples have similar microspheres built with nanosheets. The transmission electron microscopy (TEM) image further reveals that CuVOH has urchin-like microspheres (inset of Figure S2a). The interplanar spacing of 11.2 Å in HRTEM image (Figure 2a) agrees well with that in between the (001) planes estimated from the XRD pattern (Figure 1b). Elements are distributed homogeneously as revealed by the energy-dispersive X-ray spectroscopy (EDS) mappings, suggesting the incorporation of Cu (II) in VOH. High resolution X-ray photoelectron spectroscopy (XPS) spectrum of V shown in Figure 2b, reveals the co-existence of both V^{5+} and V^{4+}, with a peak at 517.5 eV from V^{5+} and a smaller peak at 516.6 eV from V^{4+} as reported.[70, 71] The amount of V^{4+} is estimated to be 17.9% in CuVOH, higher than the 13.2% in VOH (Figure S3). The formation of V^{4+} in VOH is possibly due to the reduction reaction happened between V_2O_5 and H_2O_2 to form $VO(O_2)^+$ in the synthesis process.[72] The chemical valence of Cu (II) is also confirmed and the peak at 933.5 eV and the strong satellite peak at 937.2 eV[73, 74] (Figure 2c) demonstrate no oxidizing reaction occurs on Cu (II). The

additional satellite peaks imply an intensive Coulombic interaction among the 3*d* electrons and the hybridization between the Cu 3*d* and other valence orbitals as observed in other TM compounds,[75-77] especially when the local chemical surrounding involves in oxygen that connects with V or H. The chemical states of V and Mg cations in MgVOH were also analyzed by XPS and spectra are shown in Figure S4. V^{4+} is detected in MgVOH and the amount is ~ 16.5% as listed in Table 1. XPS spectrum of elemental Mg indicates that its chemical valence keeps at 2+, confirming that they are chemically stable in the hydrothermal process. Both samples have a similar amount of V^{4+}. The chemical surroundings and states of V cations in the bulk samples are tested by means of X-ray absorption near edge structure (XANES) and the spectra are shown in Figure 2d. The peak appeared in the pre-edge region correspond to the coordination symmetry of the metal ion center and their intensities also reflect the degree of unoccupied d orbitals.[78, 79] VO_2 as an empirical standard built by highly symmetric [VO_6] octahedron and fewer unoccupied d orbitals present in V^{4+}, resulting in a lower intensity. While V_2O_5 consists of asymmetric [VO_5] pyramids and V^{5+} contains more unoccupied d orbitals, it exhibits a higher pre-edge intensity. The intensity of VOH sits between those of VO_2 and V_2O_5, agreeing with its structure consisted of symmetric [VO_6] octahedron and asymmetric [VO_5] pyramids alternately. The intensities of MgVOH and CuVOH are higher than those of VOH and V_2O_5, demonstrating more serious lattice distortion in both samples because of the introduction of alien cation and the formation of strong chemical bonds as verified by Raman analysis. CuVOH presents a slightly higher intensity that is in accord with the difference in the amount of V^{4+} tested by XPS since the larger size V^{4+} in the lattice causes more serious lattice distortion.[80] The K-edge position reflects the chemical states of V cations, three samples have the similar K-edge positions with the empirical standard V_2O_5, suggesting V^{5+} dominates their chemical states. However, a slight shift toward lower photo energy confirms the

formation of V^{4+} in CuVOH and MgVOH bulks in comparison with VOH as verified by XPS. Thermogravimetric analysis (TGA) was performed with a temperature range of 30-700 ˚C to evaluate the water content in the resulting samples (Figure 2e). CuVOH has the lowest water content of 14.2 *wt*%, MgVOH is 16.0 *wt*% and VOH has the highest one of 16.7 *wt*%. Considering the measurement deviation, it would be thought three resulting samples have a close water content. These results demonstrate CuVOH and MgVOH possess similar crystal structures and chemical states, and the possible influences from water on their electrochemical performance would be excluded.

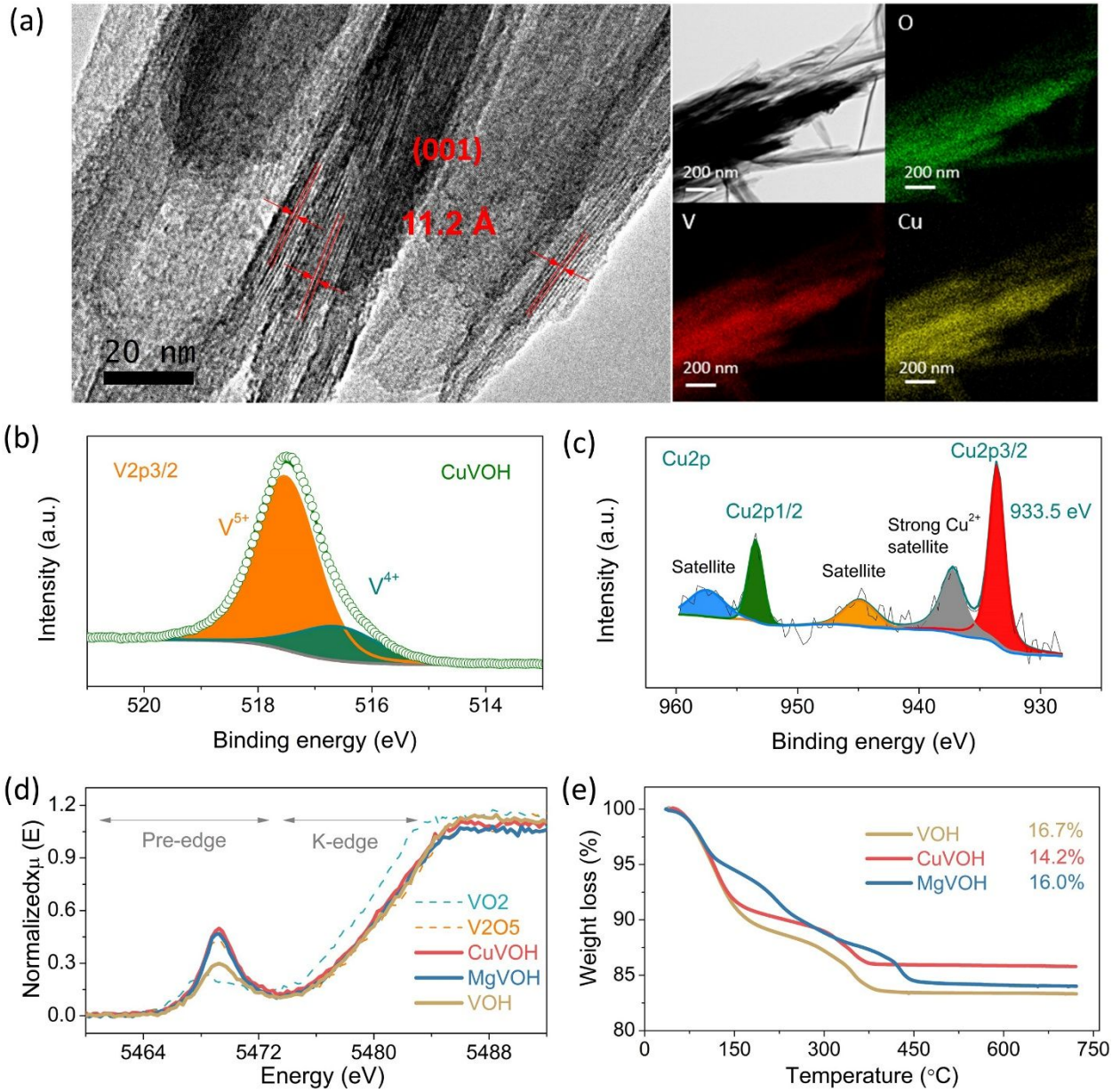

Figure 2. (a) HRTEM images with the corresponding EDS mappings of CuVOH. The microspheres consist of nanosheets; the lattice spacing is 11.2 Å that corroborates well with the XRD results. The elements distribute homogenously in the nanosheets. XPS spectra of (b) V and (c) Cu collected from CuVOH. The appearance of V^{4+} suggests the incomplete oxidation of V^{5+} and the formation of oxygen vacancies. Cu (II) with strong satellite peaks were detected owing to its different local chemical surroundings. (d) Normalized V K-edge XANES spectra of resulting samples and standard VO_2 and V_2O_5 references. The stronger peak intensities in pre-edge zone reflect a lattice distortion in MgVOH and CuVOH compared with the symmetric coordination in VO_2. (e) TGA curves of the resulting samples collected with a temperature of 30-700 ˚C. Three resulting sample have a close water content around 16 *wt*%.

Cyclic Voltammetry (CV) curves are shown in Figure 3a and two pairs of redox peaks appear within the operating voltage window of 0.2-1.6 V at a sweep rate of 0.1 mV/s. One pair of peaks around 1.0 V corresponds to the redox reaction of V^{5+}/ V^{4+} and the other appears at 0.5 V that comes from the redox pair of V^{4+}/V^{3+}, similar to those observed in V_2O_5 or $V_2O_5{\cdot}nH_2O$.[26, 29] In the first cathodic process of CuVOH (Figure S5), the first reduction peak appears at 0.96 V, but shifts to 0.98 V in subsequent cycles. This phenomenon is often observed in vanadates when zinc- or lithium-ions are intercalated, and commonly ascribed to a slight structural distortion because of the ion insertion or the activation of the fresh electrode.[34, 81] The overlap of the second and third cycles implies a high redox reversibility in the CuVOH cathode. The third cycles in the CV curves are used to compare the differences among the samples, and voltage gaps of the redox pairs in all samples are shown in Figure 3b. The possible redox reaction related to Cu (II) would make confusing in the working voltage window because Cu (II) will participate in the electrochemical reaction.[82] In fact, Cu (II) in CuO converts to Cu and Cu_2O in the first cycle and then protons insert/extract Cu_2O in the following cycles rather than zinc ions[82] because sufficient protons in the electrolyte of 3M $ZnSO_4$ aqueous solution (pH<5.4).[83] In addition, the anodic reaction of Cu^{+}/Cu^{0} happens around 1.0 V and the cathodic reaction occurs at 0.7 V, leading to a serious voltage hysteresis. While CuVOH cathode displays a decreased voltage difference for V^{5+}/V^{4+} of 0.02 V, which is lower than the 0.27 V of MgVOH and 0.25 V of VOH. The reduced voltage difference in CuVOH further verifies that the introduced Cu^{2+} possibly would not participate in the redox process. An interesting phenomenon is that the V^{5+}/V^{4+} redox pairs exhibit a slightly smaller voltage gap of 0.02 V than the V^{4+}/V^{3+} redox pair (0.07 V) in the CuVOH cathode. One possible reason is less Zn^{2+} insert the host lattice corresponding to the V^{5+}/V^{4+} redox pairs and

more sufficient channels for ion diffusion at this stage. The other is V^{4+} and V^{3+} have larger ionic radii of 72 and 78 pm in a six-coordination than that (68 pm) of V^{5+} in the same surroundings,[84] the larger ionic radii of cations distributed in the layers randomly block the Zn ion migration, leading to a high energy barrier for Zn-ion diffusion and slower reaction kinetics. To further explore the functions of the Cu (II) cation, potentiostatic polarization curves were tested at a sweep rate of 0.1 mV/s (Figure S6) and the corresponding Tafel curves are plotted as shown in Figure 3c. The slopes of Tafel curves decreases from 295 mV/dec of VOH, 297 mV/dec of MgVOH to 268 mV/dec of CuVOH, and the corresponding exchange current density increase from 0.20 A/g of VOH and 0.19 A/g of MgVOH to 0.23 A/g of Cu VOH. The enhanced current density can be attributed to a catalytic effect of Cu (II) cations on promoting the zinc-ion storage reaction because the partially unfilled 3*d* orbitals of transition metal cations can capture and transfer electrons to accelerate the redox reaction. Elemental Cu has an electronegativity of 1.90 Pauling units, while Mg element is 1.31 Pauling units. The covalent character of chemical bonds consisted of cations and oxygen in a compound can be evaluated by the following equation,[75]

$$\% \text{ covalent character} = 100 \times \exp\left[-0.25 \left(X_M - X_O\right)^2\right] \quad (1)$$

where X_M and X_O are Pauling electronegativities of metallic and oxygen (3.44 Pauling units) elements, respectively. The covalent character in Cu-O bond is 55% in CuVOH, while it is around 32% in Mg-O bond. A higher covalence character in the chemical bond enables a stronger catalytic effect owing to the highly electron sharing and feasible electron transfer in the reaction process.[85, 86] To further confirm the catalytic effect of Cu (II), EIS spectra in Figure 3d compare the charge transfer resistances, CuVOH has the smallest resistance of 16 Ω in comparison with 40 Ω of VOH

and 59 Ω of MgVOH, agreeing with the enhanced the reaction kinetic disclosed by CV curves. The linear relationship between frequency and real resistance in Figure S7 reveals the ion diffusion coefficients of three samples, CuVOH presents the highest ion diffusion coefficient of 15.5×10^{-13} cm^2/s than 3.3×10^{-13} cm^2/s of VOH and 2.0×10^{-13} cm^2/s of MgVOH. The enhanced reaction kinetics, manifested by the exchange current density, charge transfer resistance and ion diffusion coefficient as listed in Table 2, demonstrate that Cu (II) with 3*d* orbitals play a role as a catalyst to accelerate Zn-ion intercalation in aqueous batteries.

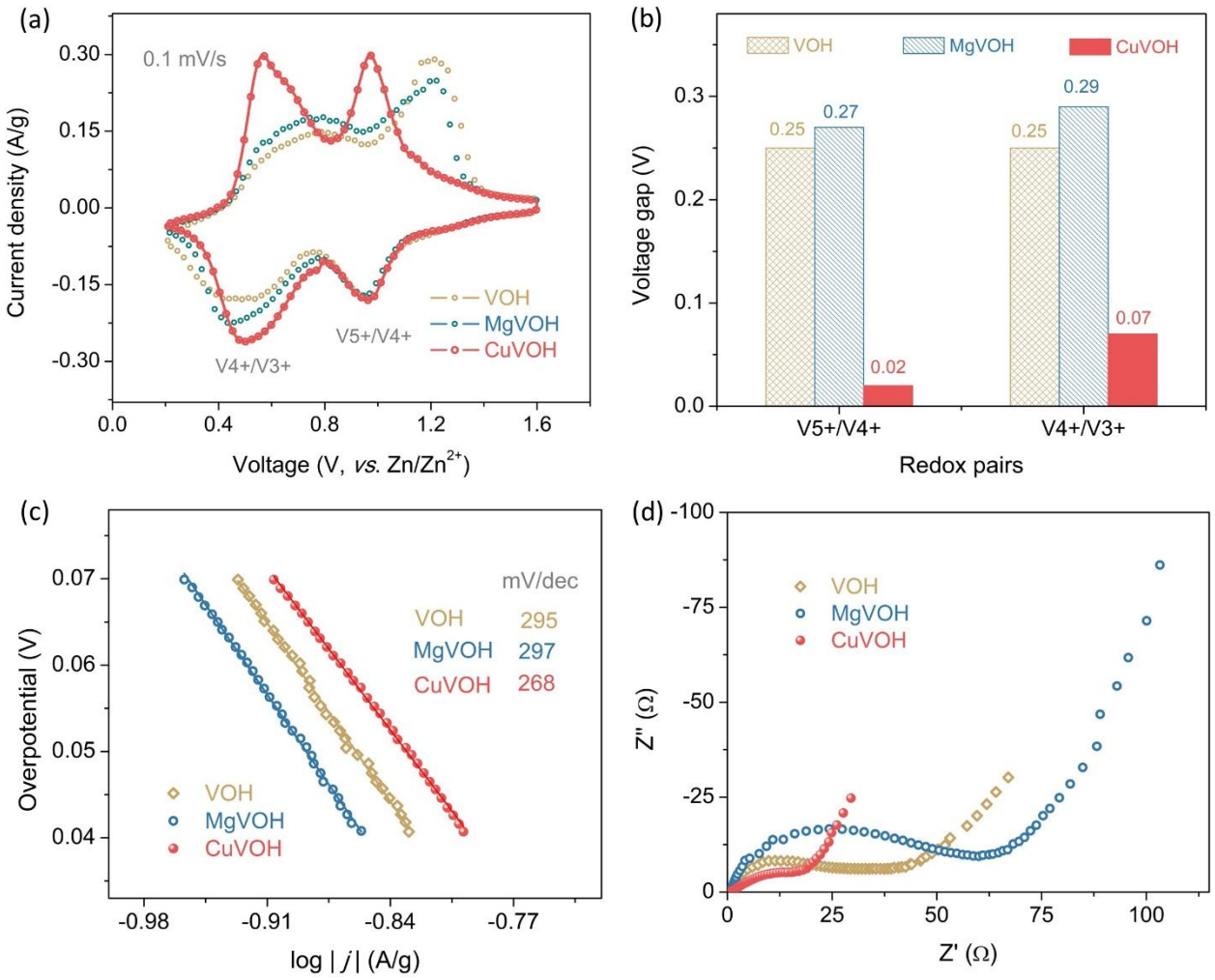

Figure 3. (a) CV curves of CuVOH cathode collected at 0.1 mV/s in an aqueous zinc ion battery. Two pairs of redox peaks originate from the redox reactions of V^{5+}/V^{4+} and V^{4+}/V^{3+}. (b) Voltage gap of the V^{5+}/V^{4+} and V^{4+}/V^{3+} redox couples in different samples and the data were collected from their CV curves tested at 0.1 mV/s. Cu (II) cations decrease the voltage gaps in comparison with that of MgVOH and VOH. (c) Tafel curves. The smaller slopes of the curves reflect a better catalytic effect for CuVOH. (d) EIS spectra of three samples.

Table 2. Comparison of electrochemical kinetics in three samples

Sample ID	VOH	MgVOH	CuVOH
Specific capacity at 0.5 A/g (mAh/g)	337	349	379
Exchange current density (A/g)	0.20	0.19	0.23
Charge transfer resistance (Ω)	40	59	16
Ion diffusion coefficient (cm^2/s)	3.3×10^{-13}	2.0×10^{-13}	1.6×10^{-12}

Figure 4a compares the rate capabilities of three cathodes, CuVOH delivers the highest specific capacity of 379 mAh/g, compared to MgVOH of 349 mAh/g and VOH of 337 mAh/g at 0.5 A/g. CuVOH achieves a capacity retention of 93% over 1000 cycles, compared to 76% of VOH and 78% of MgVOH (Figure 4b), much better than data reported in the literature listed in Table S1. Figure 4c shows the voltage hysteresis of three cathodes at 8 A/g and the areas encompassed by the charging and discharging curves are the energy loss in each charge-discharge cycle. The small hysteresis in CuVOH corroborates with the narrow voltage gap observed in the CV curve in Figure 3a-b, resulting in a much higher energy conversion efficiency than those of both MgVOH and VOH. Energy efficiency (EE) is defined by the ratio of discharged and charged energy density of a given battery and reflects the energy conversion loss causing by polarization and side

reactions in practice [87]. Figure 4d compares the EEs of batteries at different current densities. At the small current density, the batteries display the similar EEs, such as 85% of MgVOH and 86% of CuVOH, because the considerably sufficient reaction happens with the thorough diffusion. When the current density increased to 8 A/g, the EE of CuVOH remains 72%, but MgVOH and VOH have the values of 55% and 53%, respectively. When the batteries were fully charged at 50 mA/g and put on the shelf for over 48 h, the voltage of CuVOH remained at 1.41 V which is higher than 1.35 V of MgVOH and VOH (Figure 4e). The maximum energy and power density of CuVOH are 286 Wh/kg and 5,600 W/kg, respectively, as shown in Figure 4f. It displays a competitive practicability comparing to MgVOH (E_{max}: 266 Wh/kg, P_{max}: 5262 W/kg), and VOH (E_{max}: 248 Wh/kg, P_{max}: 5261 W/kg) as well as reported results (α-MnO_2, [88] ZnHCF [89] and $Zn_{0.25}V_2O_5{\cdot}nH_2O$ [49]). In their crystal structures, CuVOH has the smallest lattice spacing of 11.2 Å among all samples, but delivers the best rate capability, suggesting that the lattice spacing is not the only limiting factor to determine the electrochemical performance of VOH.

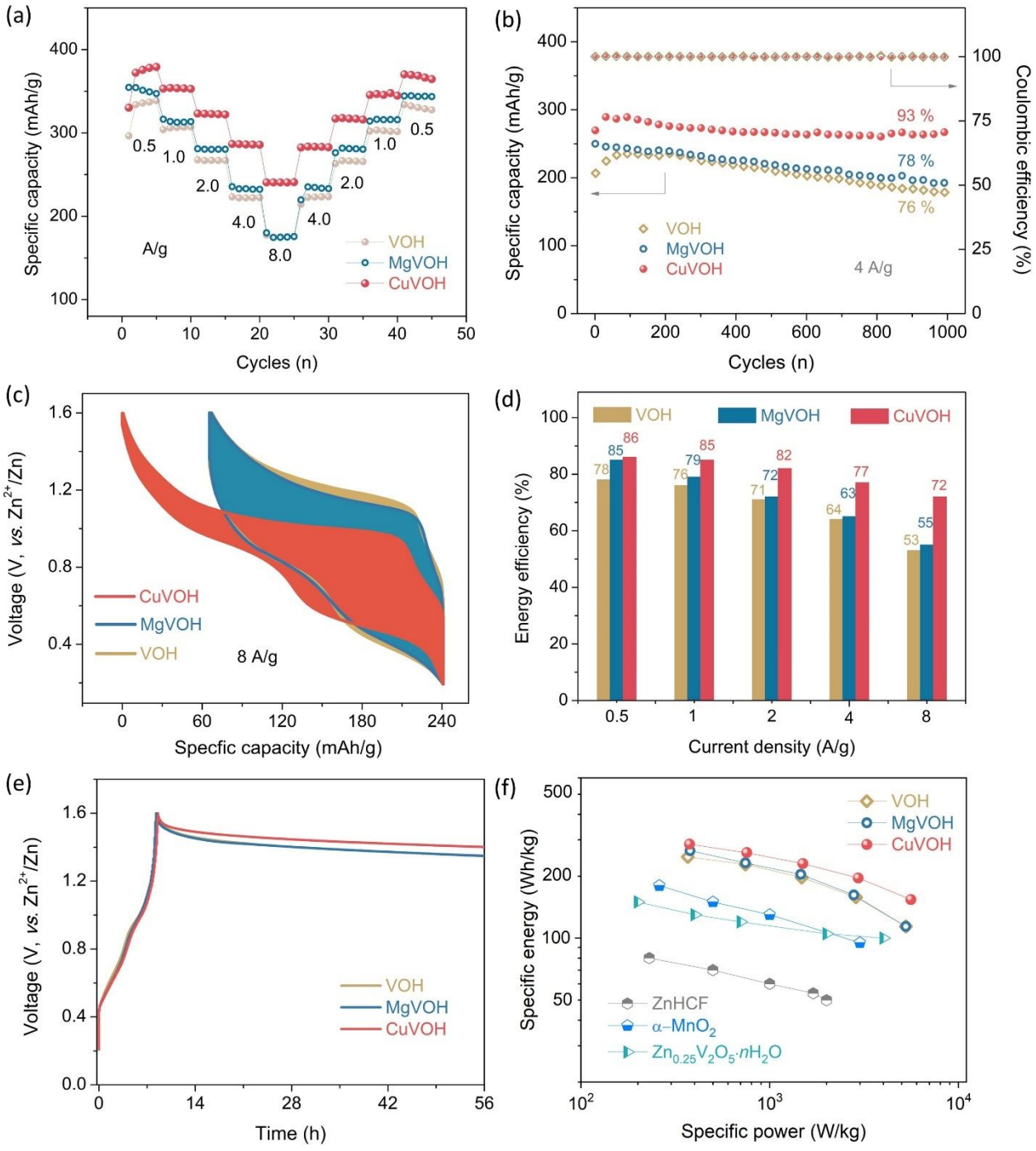

Figure 4. (a) Rate capabilities and (b) Cycling stabilities with the corresponding Coulombic efficiencies at 4 A/g for all cathodes. The improved rate capabilities and enhanced capacities are attributed to the stabilized crystal structure and catalytic effect enabled by the Cu (II) cations. (c) Voltage hysteresis of the cathodes collected at 8 A/g. The area encompassed by the charge/discharge curves is the energy loss in one cycle. (d) Comparison of energy efficiencies at different rates. MgVOH and VOH present similar EE at the same condition, but CuVOH has the highest efficiency, suggesting a catalytic effect from transition metal cation Cu (II) that promotes the efficient redox reactions. (e) Voltage degradation after being fully charged.

CuVOH presents a higher voltage retention after 48 h on the shelf. (f) Ragone plots of the cathodes in this study compared with the reported results (α-MnO_2, [88] ZnHCF [89] and $Zn_{0.25}V_2O_5{\cdot}nH_2O$ [49]).

To further confirm the catalytic effect, the reaction resistance and mechanism of both samples are studied through the galvanostatic intermittent titration technique (GITT) and ex-situ XRD tests. The relaxation rest after charging and discharging process causes the zigzag profiles in the GITT plot (Figure 5a), and the voltage recovery is usually used to estimate the ion diffusion and IR drop reflects the reaction resistances.[56] Based on the GITT curves, the diffusion coefficient of zinc ion in the material can be calculated by the following equation[47]:

$$D_{Zn^{2+}} = \frac{4}{\pi}\left(\frac{n_M V_M}{S}\right)^2\left[\frac{\Delta E_S}{\tau\left(\frac{dE_\tau}{d\sqrt{\tau}}\right)}\right]^2 \quad (\tau \ll L^2/D_{Zn^{2+}}) \tag{1}$$

where τ is the interval of 10 min for each step; n_M and V_M are the moles (mol) of the material and molar volume (cm^3/mol), respectively; S is the electrode-electrolyte contact area (cm^2); ΔE_s and ΔE_τ are the change of the steady state voltage and overall cell voltage after applying a current pulse in a single step without iR drop, respectively. L is the thickness of the electrode. When the variation of the voltage (ΔE_τ) in the titration process was found to show a linear relationship against $\tau^{1/2}$, the equation can be simplified as below,[47]

$$D_{Zn^{2+}} = \frac{4}{\pi}\left(\frac{n_M V_M}{S}\right)^2\left[\frac{\Delta E_S}{\Delta E_\tau}\right]^2 \tag{2}$$

Molar volume is one of most important parameters for the calculation of diffusion coefficient. However, the studies on crystal structure of the resulting samples by synchrotron radiation techniques are confronted with the challenges from the vanadium and water. To avoid a misleading comparison among three samples, diffusion coefficients from GITT at current stage

would not be calculated. By contrast, EIS collected at the same conditions are reasonable[90] for comparing their diffusion as listed in Table 2. In addition, VOH presents the largest IR drop and highest charging voltage, implying the sluggish reaction kinetics. Cu (II) and Mg(II) connects the [VO_n] layers to build a three-dimensional network for charge transfer compared to the two-dimensional VOH. But the ionically dominated Mg-O bonds localizes the electrons and a stronger electrostatic attraction suppresses the electron transfer, resulting in a higher IR in comparison with that of CuVOH as shown in Figure S8, and agreeing with the smallest charge transfer resistance in Figure 3e and Table 2. The phases at fully discharged and charged states were checked by ex-situ XRD measurements (Figures 5b-c), and the pristine phase can be totally recovered in the fully charged states. In the fully discharged state, several peaks appeared because of the highly ordered layers stacking formed by the strong chemical connection built by intercalated Zn ions. The additional peaks can be indexed well with the preinserted VOH as reported.[47] A slight distinction is that the (001) peak in CuVOH shifts to lower angles and a weaker peak intensity shows in MgVOH. The possible reason can be attributed to the characters of chemical bonds. Covalently dominated Cu-O bonds enable the lattice flexibility to accommodate the volume expansion without crystallinity damage, while the ionically dominated Mg-O bonds easily lose the buffering function when zinc ion inserted. It is consistent with the cycling stability at high rate of 4 A/g in Figure 4b. The reversible phase transition with the similar intercalation mechanism in both cathodes and the different electrochemical performance further indicate a catalytic effect from the special electron structure of Cu (II). The partially unfilled 3*d* orbitals can capture and transfer electrons in redox reactions as expected from a catalytic function and promote the Zn-ion storage reaction kinetics in aqueous batteries.

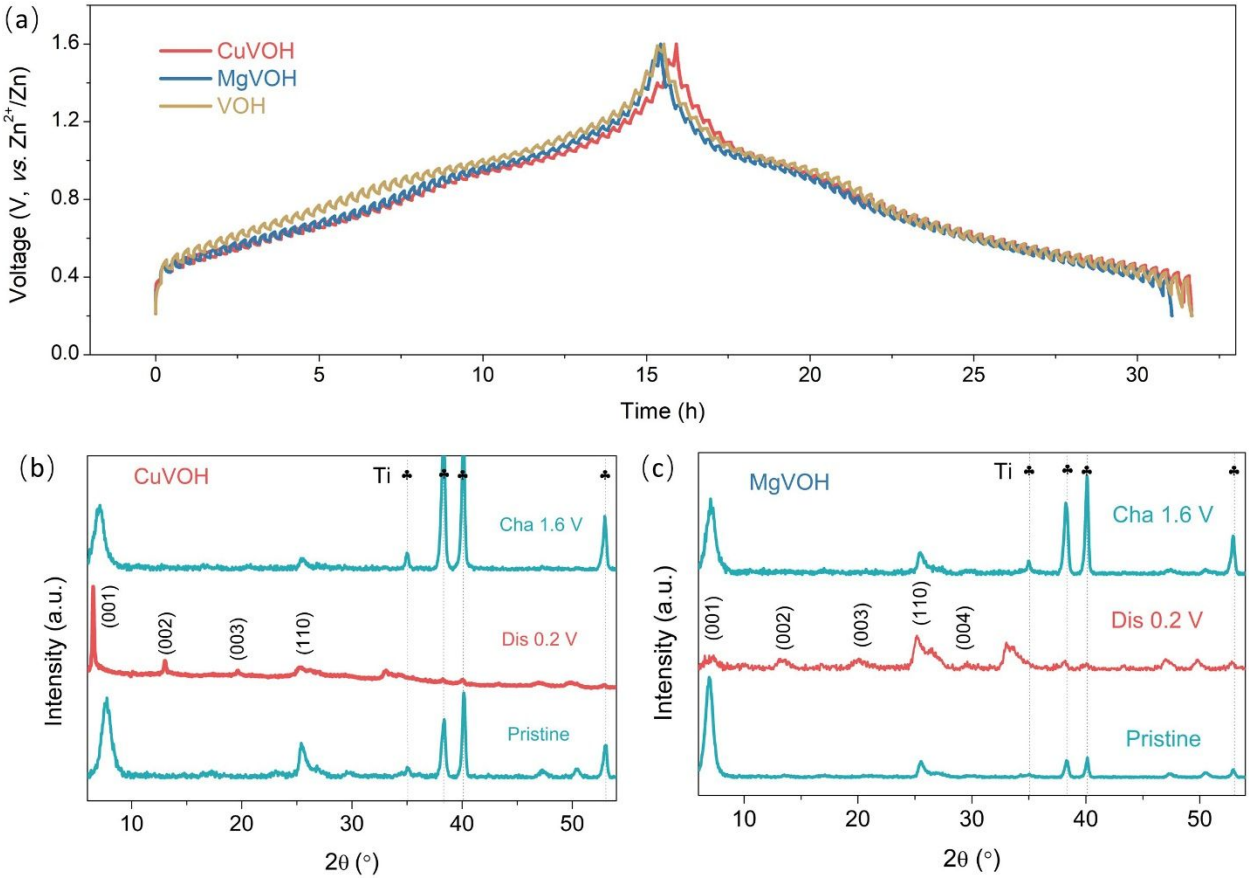

Figure 5. (a) GITT plot of the cathodes collected at a current density of 50 mA/g with a charge/discharge time and interval of 10 min for each step. Ex-situ XRD patterns of (b) CuVOH and (c) MgVOH, the phase evolution suggests the similar phase transition happened in both cathodes in the charge/discharge process.

Conclusions

Chemically pre-inserted divalent Cu and Mg in hydrated vanadium pentoxides form chemical bonds connect the adjacent [VO_5] layers and render a robust framework for reversible zinc ion intercalation. The enhanced exchange current density and reduced charge transfer resistance and increased covalent character in CuVOH as compared to MgVOH and VOH result in improved

rate capability, reduced voltage gap and enhanced energy efficiency. CuVOH offers a specific capacity of 379 mAh/g, as compared to 349 mAh/g of MgVOH and 337 mAh/g of VOH at 0.5 A/g. In distinct contrast, pre-inserted Mg has exerted limited influence on the electrochemical properties and batteries performance. Much enhanced electrochemical properties and battery performance of CuVOH, which are likely attributed to catalytic effects of the transition metal cation, Cu (II). This strategy is effective and efficient for designing and exploring high-performance cathode materials for multi-valent ion batteries.

Acknowledgements

This work was supported by the National Science Foundation (CBET-1803256). Part of this work was conducted at the Molecular Analysis Facility, a National Nanotechnology Coordinated Infrastructure site at the University of Washington which is supported in part by the National Science Foundation (grant NNCI-1542101), the University of Washington, the Molecular Engineering & Sciences Institute, and the Clean Energy Institute. CL appreciates Neware Battery Testing Instruments for providing the technical support. MY and JY acknowledge the support from The Clean Energy Institute (CEI) at the University of Washington and the Inamori Foundation.

References

1 S. Chu, Y. Cui and N. Liu, *Nat. Mater.*, 2016, **16**, 16-22.

2 G. Crabtree, *Nature*, 2015, **526**, S92.

3 Z. P. Cano, D. Banham, S. Ye, A. Hintennach, J. Lu, M. Fowler and Z. Chen, *Nat. Energy*, 2018, **3**, 279-289.

4 P. Simon, Y. Gogotsi and B. Dunn, *Science*, 2014, **343**, 1210-1211.

5 M. Winter and R. J. Brodd, *Chem. Rev.*, 2004, **104**, 4245-4270.

6 C. Liu, Z. G. Neale and G. Cao, *Mater. Today*, 2016, **19**, 109-123.

7 C. Liu, F. Li, L.P. Ma and H.M. Cheng, *Adv. Mater.*, 2010, **22**, E28-E62.

8 C. M. Hayner, X. Zhao and H. H. Kung, *Ann. Rev. Chem. Biomol. Eng.*, 2012, **3**, 445-471.

9 K. Liu, Y. Liu, D. Lin, A. Pei and Y. Cui, *Sci. Adv.*, 2018, **4**, eaas9820.

10 C. Liu, J. Yuan, R. Masse, X. Jia, W. Bi, Z. Neale, T. Shen, M. Xu, M. Tian, J. Zheng, J. Tian and G. Cao, *Adv. Mater.*, 2020, DOI:10.1002/adma.201905245.

11 A. Konarov, N. Voronina, J. H. Jo, Z. Bakenov, Y.K. Sun and S.T. Myung, *ACS Energy Lett.*, 2018, **3**, 2620-2640.

12 Y. Li, J. Fu, C. Zhong, T. Wu, Z. Chen, W. Hu, K. Amine and J. Lu, *Adv. Energy Mater.*, 2019, **9**, 1802605.

13 J. F. Parker, J. S. Ko, D. R. Rolison and J. W. Long, *Joule*, 2018, **2**, 2519-2527.

14 Y. Liu, C. Li, J. Xu, M. Ou, C. Fang, S. Sun, Y. Qiu, J. Peng, G. Lu, Q. Li, J. Han and Y. Huang, *Nano Energy*, 2019, **67**, 104211.

15 H. Pan, Y. Shao, P. Yan, Y. Cheng, K. S. Han, Z. Nie, C. Wang, J. Yang, X. Li, P. Bhattacharya, K. T. Mueller and J. Liu, *Nat. Energy*, 2016, **1**, 16039.

16 L. Wang, X. Cao, L. Xu, J. Chen and J. Zheng, *ACS Sustain. Chem. Eng.*, 2018, **6**, 16055-16063.

17 Y. Fu, Q. Wei, G. Zhang, X. Wang, J. Zhang, Y. Hu, D. Wang, L. Zuin, T. Zhou, Y. Wu and S. Sun, *Adv. Energy Mater.*, 2018, **8**, 1801445.

18 B. Lee, H. R. Lee, H. Kim, K. Y. Chung, B. W. Cho and S. H. Oh, *Chem. Commun.*, 2015, **51**, 9265-9268.

19 M. Chamoun, W. R. Brant, C.W. Tai, G. Karlsson and D. Noréus, *Energy Storage Materials*, 2018, **15**, 351-360.

20 S. Islam, M. H. Alfaruqi, V. Mathew, J. Song, S. Kim, S. Kim, J. Jo, J. P. Baboo, D. T. Pham, D. Y. Putro, Y.K. Sun and J. Kim, *J. Mater. Chem. A*, 2017, **5**, 23299-23309.

21 C. Zhu, G. Fang, J. Zhou, J. Guo, Z. Wang, C. Wang, J. Li, Y. Tang and S. Liang, *J. Mater. Chem. A*, 2018, **6**, 9677-9683.

22 W. Sun, F. Wang, S. Hou, C. Yang, X. Fan, Z. Ma, T. Gao, F. Han, R. Hu, M. Zhu and C. Wang, *J. Am. Chem. Soc.*, 2017, **139**, 9775-9778.

23 G. G. Yadav, J. W. Gallaway, D. E. Turney, M. Nyce, J. Huang, X. Wei and S. Banerjee, *Nat. Commun.*, 2017, **8**, 14424.

24 G. Liu, H. Huang, R. Bi, X. Xiao, T. Ma and L. Zhang, *J. Mater. Chem. A*, 2019, **7**, 20806-20812.

25 P. Hu, M. Yan, T. Zhu, X. Wang, X. Wei, J. Li, L. Zhou, Z. Li, L. Chen and L. Mai, *ACS Appl. Mater. Interfaces*, 2017, **9**, 42717-42722.

26 N. Zhang, Y. Dong, M. Jia, X. Bian, Y. Wang, M. Qiu, J. Xu, Y. Liu, L. Jiao and F. Cheng, *ACS Energy Lett.*, 2018, **3**, 1366-1372.

27 Q. Pang, C. Sun, Y. Yu, K. Zhao, Z. Zhang, M. Voyles Paul, G. Chen, Y. Wei and X. Wang, *Adv. Energy Mater*, 2018, **8**, 1800144.

28 P. Senguttuvan, S.D. Han, S. Kim, A. L. Lipson, S. Tepavcevic, T. T. Fister, I. D. Bloom, A. K. Burrell and C. S. Johnson, *Adv. Energy Mater.*, 2016, **6**, 1600826.

29 M. Yan, P. He, Y. Chen, S. Wang, Q. Wei, K. Zhao, X. Xu, Q. An, Y. Shuang, Y. Shao, K. T. Mueller, L. Mai, J. Liu and J. Yang, *Adv. Mater.*, 2018, **30**, 1703725.

30 L. Chen, Y. Ruan, G. Zhang, Q. Wei, Y. Jiang, T. Xiong, P. He, W. Yang, M. Yan, Q. An and L. Mai, *Chem. Mater.*, 2019, **31**, 699-706.

31 Y. Yang, Y. Tang, G. Fang, L. Shan, J. Guo, W. Zhang, C. Wang, L. Wang, J. Zhou and S. Liang, *Energy Environ. Sci.*, 2018, **11**, 3157-3162

32 X. Dai, F. Wan, L. Zhang, H. Cao and Z. Niu, *Energy Storage Materials*, 2018, **17**, 143-150.

33 P. Hu, T. Zhu, X. Wang, X. Wei, M. Yan, J. Li, W. Luo, W. Yang, W. Zhang, L. Zhou, Z. Zhou and L. Mai, *Nano Lett.*, 2018, **18**, 1758-1763.

34 V. Soundharrajan, B. Sambandam, S. Kim, M. H. Alfaruqi, D. Y. Putro, J. Jo, S. Kim, V. Mathew, Y.K. Sun and J. Kim, *Nano Lett.*, 2018, **18**, 2402-2410.

35 Z. Liu, G. Pulletikurthi and F. Endres, *ACS Appl. Mater. Interfaces*, 2016, **8**, 12158-12164.

36 R. Trócoli and F. La Mantia, *Chemsuschem*, 2015, **8**, 481-485.

37 G. Kasiri, R. Trócoli, A. Bani Hashemi and F. La Mantia, *Electrochim. Acta*, 2016, **222**, 74-83.

38 L. Zhang, L. Chen, X. Zhou and Z. Liu, *Sci. Rep.*, 2015, **5**, 18263.

39 H. Li, Q. Yang, F. Mo, G. Liang, Z. Liu, Z. Tang, L. Ma, J. Liu, Z. Shi and C. Zhi, *Energy Storage Materials*, 2019, **19**, 94-101.

40 T. Jiao, Q. Yang, S. Wu, Z. Wang, D. Chen, D. Shen, B. Liu, J. Cheng, H. Li, L. Ma, C. Zhi and W. Zhang, *J. Mater. Chem. A*, 2019, **7**, 16330-16338.

41 W. Xu, C. Sun, K. Zhao, X. Cheng, S. Rawal, Y. Xu and Y. Wang, *Energy Storage Materials*, 2019, **16**, 527-534.

42 Q. Zhao, W. Huang, Z. Luo, L. Liu, Y. Lu, Y. Li, L. Li, J. Hu, H. Ma and J. Chen, *Sci. Adv.*, 2018, **4**, eaao1761.

43 B. Tang, L. Shan, S. Liang and J. Zhou, *Energy Environ. Sci.*, 2019, **12**, 3288-3304.

44 M. Song, H. Tan, D. Chao and H. J. Fan, *Adv. Funct. Mater.*, 2018, **28**, 1802564.

45 G. Fang, C. Zhu, M. Chen, J. Zhou, B. Tang, X. Cao, X. Zheng, A. Pan and S. Liang, *Adv. Funct. Mater.*, 2019, **29**, 1808375.

46 S. Zhao, B. Han, D. Zhang, Q. Huang, L. Xiao, L. Chen, D. G. Ivey, Y. Deng and W. Wei, *J. Mater. Chem. A*, 2018, **6**, 5733-5739.

47 F. Ming, H. Liang, Y. Lei, S. Kandambeth, M. Eddaoudi and H. N. Alshareef, *ACS Energy Lett.*, 2018, **3**, 2602-2609.

48 X. Guo, G. Fang, W. Zhang, J. Zhou, L. Shan, L. Wang, C. Wang, T. Lin, Y. Tang and S. Liang, *Adv. Energy Mater.*, 2018, **8**, 1801819.

49 D. Kundu, B. D. Adams, V. Duffort, S. H. Vajargah and L. F. Nazar, *Nat. Energy*, 2016, **1**, 16119.

50 D. Chao, C. Zhu, M. Song, P. Liang, X. Zhang, N. H. Tiep, H. Zhao, J. Wang, R. Wang, H. Zhang and H. J. Fan, *Adv. Mater.*, 2018, **30**, 1803181.

51 T. Wu, K. Zhu, C. Qin and K. Huang, *J. Mater. Chem. A*, 2019, **7**, 5612-5620.

52 J. Zheng, C. Liu, M. Tian, X. Jia, E. P. Jahrman, G. T. Seidler, S. Zhang, Y. Liu, Y. Zhang, C. Meng and G. Cao, *Nano Energy*, 2020, **70**, 104519.

53 Y. Wang, J. Li and Z. Wei, *J. Mater. Chem. A*, 2018, **6**, 8194-8209.

54 J. He, G. Hartmann, M. Lee, G. S. Hwang, Y. Chen and A. Manthiram, *Energy Environ. Sci.*, 2019, **12**, 344-350.

55 H. Al Salem, G. Babu, C. V. Rao and L. M. R. Arava, *J. Am. Chem. Soc.*, 2015, **137**, 11542-11545.

56 C. Liu, G. Z. Neale, J. Zheng, X. Jia, J. Huang, M. Yan, M. Tian, M. Wang, J. Yang and G. Cao, *Energy Environ. Sci.*, 2019, **12**, 2273-2285.

57 V. Petkov, P. N. Trikalitis, E. S. Bozin, S. J. L. Billinge, T. Vogt and M. G. Kanatzidis, *J. Am. Chem. Soc.*, 2002, **124**, 10157-10162.

58 C. C. Torardi, C. R. Miao, M. E. Lewittes and Z. Li, *J. Solid State Chem.*, 2002, **163**, 93-99.

59 E. Potiron, A. Le Gal La Salle, A. Verbaere, Y. Piffard, D. Guyomard and M. Tournoux, *J. Phys. Chem. Solids*, 2001, **62**, 1447-1455.

60 E. Potiron, A. Le Gal La Salle, A. Verbaere, Y. Piffard and D. Guyomard, *Electrochim. Acta*, 1999, **45**, 197-214.

61 C. L. Londoño-Calderón, C. Vargas-Hernández and J. F. Jurado, *Rev. mex. de fís.*, 2010, **56**, 411-415.

62 S. Boukhalfa, K. Evanoff and G. Yushin, *Energy Environ. Sci.*, 2012, **5**, 6872-6879.

63 J. Yao, Y. Li, R. C. Massé, E. Uchaker and G. Cao, *Energy Storage Materials*, 2018, **11**, 205-259.

64 J. Lee, S. Badie, P. Srimuk, A. Ridder, H. Shim, S. Choudhury, Y.C. Nah and V. Presser, *Sustain. Energy & Fuels*, 2018, **2**, 577-588.

65 Y. Deng, A. D. Handoko, Y. Du, S. Xi and B. S. Yeo, *ACS Catalysis*, 2016, **6**, 2473-2481.

66 J. F. Xu, W. Ji, Z. X. Shen, W. S. Li, S. H. Tang, X. R. Ye, D. Z. Jia and X. Q. Xin, *J. Raman Spectrosc.*, 1999, **30**, 413-415.

67 H. Hagemann, H. Bill, W. sadowski, E. Walker and M. François, *Solid State Commun.*, 1990, **73**, 447-451.

68 J. Livage, *Chem. Mater.*, 1991, **3**, 578-593.

69 G. H. Jaffari, A. Tahir, M. Bah, A. Ali, A. S. Bhatti and S. I. Shah, *J. Phys. Chem. C*, 2015, **119**, 28182-28189.

70 E. Hryha, E. Rutqvist and L. Nyborg, *Surf. Interface Anal.*, 2012, **44**, 1022-1025.

71 M. Demeter, M. Neumann and W. Reichelt, *Surf. Sci.*, 2000, **454-456**, 41-44.

72 C. Li, P. Zheng, J. Li, H. Zhang, Y. Cui, Q. Shao, X. Ji, J. Zhang, P. Zhao and Y. Xu, *Angew. Chem. Int. Edit*, 2003, **42**, 5063-5066.

73 D. Barreca, A. Gasparotto and E. Tondello, *Surf. Sci. Spectra*, 2007, **14**, 41-51.

74 *http://www.xpsfitting.com/2012/01/copper.html*.

75 C. Liu, C. Zhang, H. Fu, X. Nan and G. Cao, *Adv. Energy Mater.*, 2017, **7**, 1601127.

76 D. Guo, Z. Wu, Y. An, X. Li, X. Guo, X. Chu, C. Sun, M. Lei, L. Li, L. Cao, P. Li and W. Tang, *J.Mater. Chem. C*, 2015, **3**, 1830-1834.

77 *https://xpssimplified.com/elements/copper.php*.

78 G. T. Seidler, D. R. Mortensen, A. J. Remesnik, J. I. Pacold, N. A. Ball, N. Barry, M. Styczinski and O. R. Hoidn, *Rev. Sci. Instrum.*, 2014, **85**, 113906.

79 E. P. Jahrman, W. M. Holden, A. S. Ditter, D. R. Mortensen, G. T. Seidler, T. T. Fister, S. A. Kozimor, L. F. J. Piper, J. Rana, N. C. Hyatt and M. C. Stennett, *Rev. Sci. Instrum.*, 2019, **90**, 024106.

80 G. A. Horrocks, E. J. Braham, Y. Liang, L. R. De Jesus, J. Jude, J. M. Velázquez, D. Prendergast and S. Banerjee, *J. Phys. Chem. C*, 2016, **120**, 23922-23932.

81 Y. Li, J. Yao, E. Uchaker, J. Yang, Y. Huang, M. Zhang and G. Cao, *Adv. Energy Mater.*, 2013, **3**, 1171-1175.

82 J. Meng, Z. Yang, L. Chen, H. Qin, F. Cui, Y. Jiang and X. Zeng, *Materials Today Energy*, 2020, **15**, 100370.

83 W. Wang and D. B. Breisinger, *Metall. Mater. Trans. B*, 1998, **29**, 1157-1166.

84 *https://www.webelements.com/atom_sizes.html*.

85 P. Sheng, C.Y. Wang, S. P. Jiang, X. Sun and J. Zhang, *Electrochemical Energy: Advanced Materials and Technologies*, CRC Press, 2015.

86 Y. Zhou, S. Sun, C. Wei, Y. Sun, P. Xi, Z. Feng and Z. J. Xu, *Adv. Mater.*, 2019, **31**, 1902509.

87 C. Liu, S. Wang, C. Zhang, H. Fu, X. Nan, Y. Yang and G. Cao, *Energy Storage Materials*, 2016, **5**, 93-102.

88 N. Zhang, F. Cheng, J. Liu, L. Wang, X. Long, X. Liu, F. Li and J. Chen, *Nat. Commun.*, 2017, **8**, 405.

89 L. Zhang, L. Chen, X. Zhou and Z. Liu, *Adv. Energy Mater.*, 2015, **5**, 1400930.

90 C. Liu, H. Fu, Y. Pei, J. Wu, V. Pisharodi, Y. Hu, G. Gao, R. J. Yang, J. Yang and G. Cao, *J. Mater. Chem. A*, 2019, **7**, 7831-7842.